Journal of Materials Chemistry A

Synergies between Electronic and Geometric Effects of Mo-doped Au Nanoparticles for Effective CO2 Electrochemical Reduction

Journal:	*Journal of Materials Chemistry A*
Manuscript ID	TA-COM-05-2020-004551.R1
Article Type:	Communication
Date Submitted by the Author:	01-Jun-2020
Complete List of Authors:	Sun, Kun; Harbin Institute of Technology, School of Chemistry and Chemical Engineering Ji, Yujin; Soochow University, Institute of Functional Nano & Soft Materials (FUNSOM) Liu, Yuanyue; University of Texas at Austin Wang, Zhijiang; Harbin Institute of Technology, School of Chemical Engineering and Technology

COMMUNICATION

Synergies between Electronic and Geometric Effects of Mo-doped Au Nanoparticles for Effective CO_2 Electrochemical Reduction

Kun Sun, †ac Yujin Ji, †de Yuanyue Liu*d and Zhijiang Wang*ab

Received 00th January 20xx,
Accepted 00th January 20xx

DOI: 10.1039/x0xx00000x

CO_2 electroreduction is developing as a promising technology to solve environmental and energy problems. Alloy catalysts with dissimilar local metal atoms induce geometric and electronic effects that may greatly contribute to their performance. However, the fundamental mechanisms for CO_2 reduction on bimetallic Au alloy surface are still ambiguous. Here, we report effective CO_2 reduction by the synergies between electronic and geometric effects on Mo-doped Au nanoparticle (MDA NP). A 97.5% CO Faradaic efficiency and 75-fold current density higher than pure Au nanoparticles were achieved at −0.4 V versus reversible hydrogen electrode for MDA NP with at least 50 h lifetime. Our experimental and theoretical calculation results reveal that the surface Au with increased electron density from Mo can effectively enhance the CO_2 activation. Moreover, the intermediate *COOH may be further stabilized by local Mo atom through additional Mo–O binding to decrease the energy barrier.

The overuse of fossil fuels leads to energy crisis and severe environmental problems due to the increasing atmospheric CO_2 concentration.[1,2] Reducing CO_2 to produce energy chemicals by using electrochemical methods can theoretically close the anthropogenic carbon cycle.[3,4] The industrial application of CO_2 electroreduction relies on the high-performance catalysts with superior selectivity and stability. Researchers worldwide have developed various transition metal catalysts for CO_2 electroreduction under ambient conditions.[5-10] Syngas (CO + H_2) is the feedstock for Fischer–Tropsch process, a technology to produce value-added chemicals and fuels.[4] Therefore, CO production via electrochemical CO_2 reduction is the most promising method to address the upcoming energy and environmental problems.[12]

Among the identified metal elements, gold (Au) represents the essential element for catalyzing CO_2 reduction to produce CO with the best selectivity.[13] The high cost and low abundance of Au are the limiting factors preventing the industrial application. Reducing the noble Au usage and improving the specific activity to meet the future application are of great importance. Hitherto, the preferable catalysts for CO production have often been produced by tuning the microstructure to expose catalytic surface,[14-17] changing the chemical composition,[10,18,19] and introducing surface strain[20]. However, these previous structural property studies are not sufficient to depict a fundamental protocol from the electronic structure level for CO_2 reduction.

In the pathway of CO production, the adsorbed CO_2 undergoes electron transfer and proton-coupled electron transfer reactions to form *COOH.[21] The sequence of rate-determining step and the ability to stabilize *COOH intermediate are the key factors in screening catalysts.[16,22] After the subsequent pathways occur, *CO is formed and desorbed as gaseous CO. For a highly selective CO catalyst, regulating the local electronic environment is vital to facilitate *COOH formation and stabilization and inhibit protons coupling to form H_2. Alloying can introduce electronic and geometric effects by using dissimilar surface atoms with the modified adsorption and stabilization property of catalysts. Sun et al. fabricated Au–Fe core-shell nanoparticle with jagged surface through surface Fe leaching, thereby showing enhanced mass activity toward CO production.[18] Pd–Au alloy, which is a representative category of catalysts, is fine-tuned surface atomic structure with improved performance; however, fundamental understanding of geometric and electronic structure of active sites is lacking.[10,23,24] General methods and mechanic insights should be developed to meet the future industrial application of Au-based electrocatalysts.

Herein, we report a new class of Mo-doped Au nanoparticle (MDA NP) with highly active, selective, and stable performance to catalyze CO_2 into CO under ambient condition. The maximum

---

[a] *MIIT Key Laboratory of Critical Materials Technology for New Energy Conversion and Storage, School of Chemistry and Chemical Engineering, Harbin Institute of Technology, Harbin 150001, China.*

[b] *State Key Laboratory of Urban Water Resource and Environment, School of Chemistry and Chemical Engineering, Harbin Institute of Technology, Harbin 150001, China.*

[c] *Department of Chemical and Biomolecular Engineering, Rice University, Houston 77005, USA.*

[d] *Texas Materials Institute and Department of Mechanical Engineering, The University of Texas at Austin, Austin 78712, USA*

[e] *Institute of Functional Nano & Soft Materials (FUNSOM), Jiangsu Key Laboratory for Carbon-Based Functional Materials & Devices, Soochow University, Suzhou 215123, China.*

* wangzhijiang@hit.edu.cn; yuanyue.liu@austin.utexas.edu

† K. Sun and Y. Ji contribute equally to this work.

Electronic Supplementary Information (ESI) available: [details of any supplementary information available should be included here]. See DOI: 10.1039/x0xx00000x

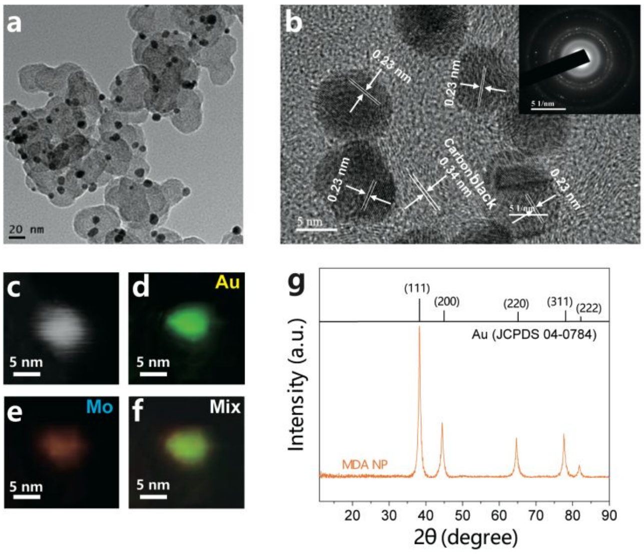

Fig. 1 (a) TEM image of MDA NP. (b) HRTEM image of MDA NP loaded on carbon black. Inset: SAED pattern. HAADF-STEM images of (c) a single MDA NP and its corresponding EDS mappings of (d) Au, (e) Mo and (f) their overlapped image. (g) X-ray diffraction patterns.

CO Faradaic efficiency (FE) reached up to 97.5% at −0.4 V versus reversible hydrogen electrode (RHE, all reported potentials are with respect to this reference) with hydrogen evolution totally suppressed which can be maintained for over 50 hours' continuous electrolysis. The CO can be detected at an onset potential as low as −0.2 V on the fabricated MDA NP. Based on density functional theory (DFT) calculations and mechanistic studies, the state-of-the-art performance achieved by MDA NP stems from the change of the surface electronic structure together with the alloy geometric effect by the Mo doping with Au.

We fabricated highly dispersed MDA NP by one-pot solvothermal method at 280 °C using gold acetate ($Au[OOCCH_3]_3$) and molybdenyl acetylacetonate ($[CH_3COCH{=}COCH_3]_2MoO_2$) as metal precursors, 1,2-hexadecanediol as reducing agent, octyl ether as solvent, and oleic acid and oleyl amine as surfactants. The gold precursor was mixed with high concentration molybdenum salt solution due to the low solubility of molybdenum in gold.[25] The high-resolution transmission electron microscope images of the MDA NP (Fig. 1a-b) revealed that the highly dispersive nanoparticles that shared the uniform sizes of 8.2±0.2 nm in diameters were supported on the carbon black substrate. Fig. 1b shows that the lattice spacing was 0.23 nm for MDA NP, which is consistent with the face-centered cubic (fcc) Au. The selected-area electron diffraction (SAED) pattern (inset of Fig. 1b) of MDA NP showed concentric rings composed of bright discrete diffraction spots, revealing the polycrystalline nature of the sample. MDA NP elemental analysis was performed with inductively coupled plasma mass spectrometry, X-ray photoelectron spectroscopy (XPS) and Energy-dispersive X-ray spectroscopy (EDS) with an atomic Mo/Au ratio of 8.7% (Table S2). The compositional distributions of Au and Mo were investigated by elemental mapping using EDS coupled with high-angle annular dark-field scanning transmission electron microscopy (HAADF-STEM). Fig. 1c shows the HAADF-STEM image of a single MDA NP. The EDS elemental maps of Au (Fig. 1d), Mo (Fig. 1e) as well as their overlapped image (Fig. 1f) were obtained in the same region. These images indicated that Au and Mo atoms were distributed uniformly in the MDA NP. X-ray diffraction measurement was performed to further examine the phase of the MDA NP (Fig. 1g). The diffraction peaks were attributed to the Au (fcc) structure, and no separate diffraction peaks for Mo species can be observed, indicating that no large clusters of the Mo phases existed, and the Mo atoms were mixed into the Au lattice.

XPS measurements of the samples were performed to investigate the electronic properties. The Au 4f and Mo 3d spectra of the MDA NP catalyst indicated the presence of Au and Mo elements in the sample. Fig. 2a shows that the peaks of MDA NP and Au NP at the binding energy about 84 eV can be assigned to metallic gold. Upon MDA NP formation, the binding energy for Au of MDA NP (83.9 eV) was decreased by 0.1 eV as compared with that of pure Au NP (84.0 eV). This finding indicated that the electron density of Au increased in the MDA NP, which is in good agreement with the electronegativity considerations between Au and Mo. Thus, charge transfer may occur between Au and Mo in MDA NP to form higher electron density of the Au in MDA NP compared with the counterpart in pure Au NP. Fig. 2b shows that Mo of MDA NP comprises of three spin-orbit split components corresponding to metallic Mo and oxidized Mo species including Mo^{4+} and Mo^{6+}, which is also in agreement with previous noble-metal alloy.[26,27] The Mo 3d spetrum for MDA NP after CO_2 electroreduction (Fig. S11) reveals an increased ratio of $Mo^0/Mo^{\delta+}$ indicating the formation of metallic Mo^0 on the particle surface during the reaction, while Mo species inside the nanoparticle still remain mixed chemical states. The surface of MDA NP is occupied by Au(111) plane based on the HRTEM and XRD analysis. We then

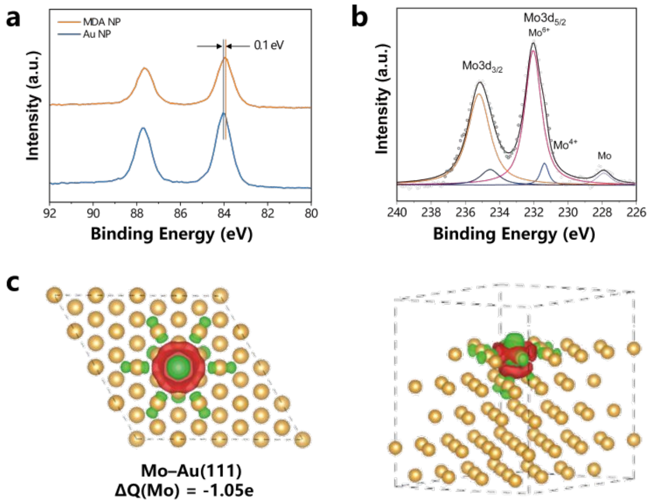

Fig. 2 (a) Au 4f XPS spectra of MDA NP and Au NP. (b) Mo 3d XPS spectra of MDA NP. (c) (Top and side views) Charge density difference of Mo-doped Au(111). The green and red colors represent the charge depletion and accumulation area, respectively. (The isosurface value is set to 0.002 e)

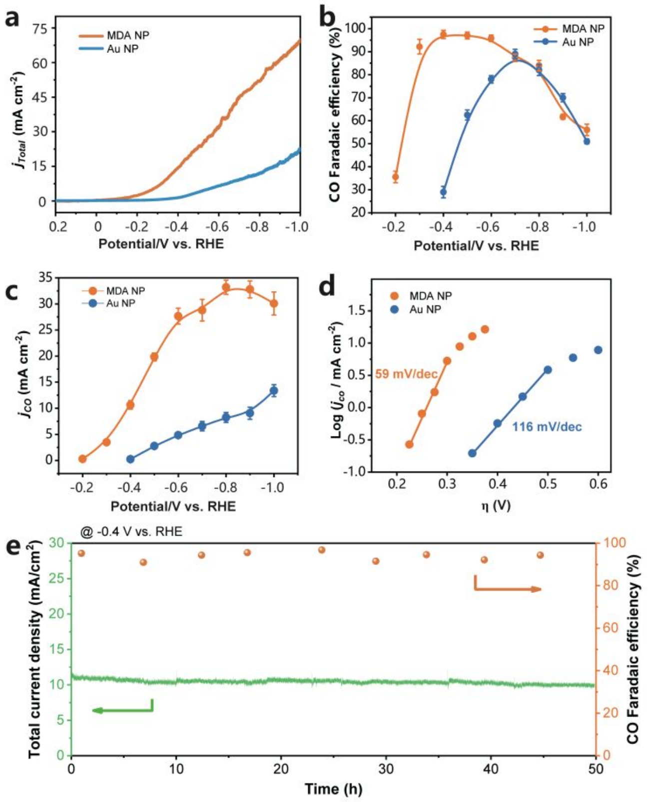

Fig. 3 (a) Linear sweep voltammetry curves of MDA NP and Au NP in CO_2-saturated 0.5M $KHCO_3$ solution. (b) Faradaic efficiencies of CO produced by MDA NP and Au NP. (c) CO Current densities of MDA NP and Au NP. (d) Tafel plots of MDA NP and Au NP. (e) Catalytic stability test of MDA NP.

conducted DFT calculations to investigate the Mo-doping effect on CO_2 reduction and construct Mo-doped Au(111) and pristine Au(111) models to represent the MDA NP and Au NP in the experiment, respectively. Fig. 2c shows that the introduction of Mo atom was energetically favorable to dope into Au(111) surface lattice and transfer the electrons to the surrounding Auatoms. According to the quantitative Bader charge analysis, the net charge transfer from Mo to Au was 1.05 e, which is in good agreement with the XPS data and also confirms the electron donor role of surface Mo.

We conducted CO_2 reduction reaction at various applied potentials in 0.5 M $KHCO_3$ solution using MDA NP and pure Au NP to evaluate the contribution in catalytic performance by Mo doping with Au. Au NP exhibited the similar shape (Fig. S1) and particle size distribution (Fig. S7) with MDA NP to rule out the influence of particle size and shape.[28,29] CO and H_2 were the only gas products detected on both catalysts from −0.2 V to −1.0 V. Shown in Fig. 3a are linear sweep voltammetry curves of MDA NP and Au NP for CO_2 electrolysis. MDA NP exhibits higher current density than Au NP. Fig. 3b shows the FE for CO production in which MDA NP yielded the highest FE for CO than Au NP at all tested potentials. When MDA NP was employed, the onset potential of CO production was at −0.2 V with considerable amounts of CO production, which was only 0.09 V below the theoretic equilibrium potential of CO_2/CO (−0.11 V). The highest FE reached 97.5% at −0.4 V with the competing HER completely suppressed, thus representing the best performance for CO_2 electroreduction among the reported Au-based catalysts at the same potential (Table S1). For pure Au NP, the onset potential was −0.4 V with a 0.2 V higher overpotential than MDA NP to actuate the CO_2 reduction. Moreover, the current density for CO production by Au NP was only 0.15 mA cm^{-2} at −0.4 V, which was nearly 75-fold smaller than that of MDA NP (11.22 mA cm^{-2}) at the same potential (Fig. 3c). These results show that MDA NP is an outstanding catalyst for CO_2 conversion into CO by substantially repressing H_2 evolution reaction.

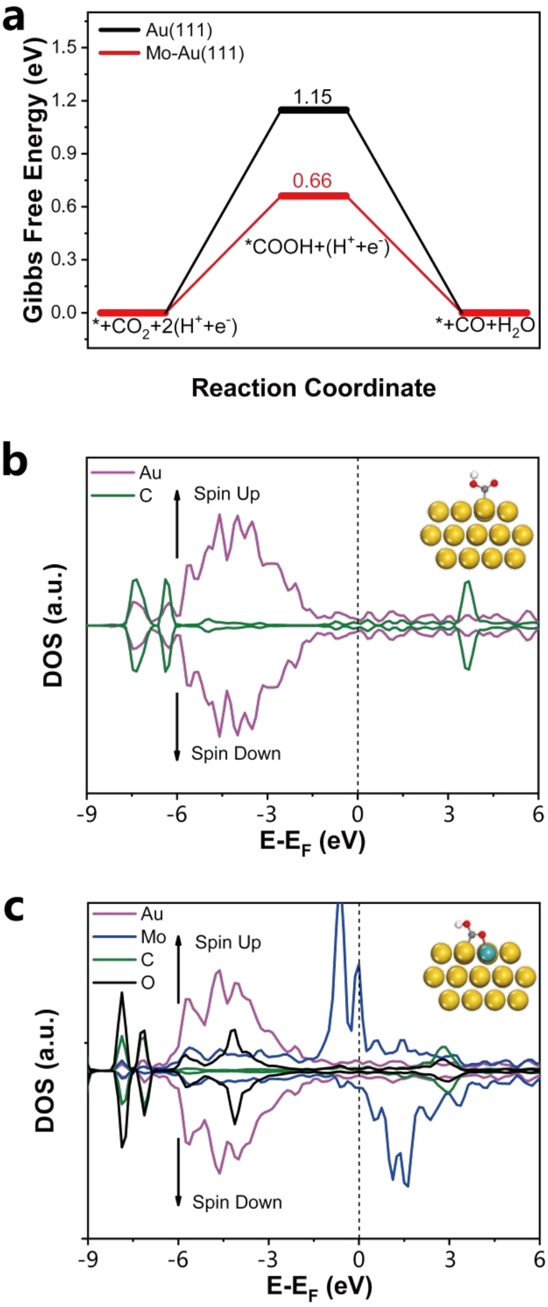

Fig. 4 (a) Free energy diagram of CO_2 reduction on Mo-doped Au(111) and Au(111). Projected density of states analysis of *COOH on (b) Au NP and (c) MDA NP. Insets show the optimized binding geometries.

Long-term electrocatalysis was performed at −0.4 V to test the operational stability of the MDA NP. Fig. 3e shows that the MDA NP catalyst possesses relative stable current density of ~10.9 mA cm^{-2} toward CO with a FE of ~96% over 50 h. The current density and selectivity of Au NP dropped dramatically during the 10 h electrolysis at −0.7 V, indicating an inferior surface stability compared with that of MDA NP (Fig. S4). Furthermore, the electrochemical surface area (ECSA) of MDA NP after 50 h of electrocatalysis remains at 95% compared with that before electrolysis, whereas only 20% ECSA remained after 10 h reaction for Au NP (Fig. S6). Thus, the MDA NP shows superior selectivity and long-term stability for CO_2 reduction. Moreover, the area-based catalystic performance based on ECSA in Fig. S8 provides the insight that the active sites in MDA NP can be further motivated by the geometric effect of Mo-doping to possess larger active surface area and specific activity compared with Au NP.

We subsequently employed Tafel analysis (Fig. 3d) to explore the kinetic mechanism of CO_2 reduction on MDA NP and Au NP. Mo-doping affects the mechanistic pathway during CO_2 electroreduction. A Tafel slope of 116 mV dec^{-1} was observed for Au NP, implying that the single electron transfer to CO_2 to form surface-adsorbed $CO_2^{\bullet-}$ is the rate-determining step in the whole reaction. By contrast, the Tafel slope for MDA NP was 59 mV dec^{-1} at relatively low overpotentials, indicating a fast one-electron transfer to CO_2 molecule as a pre-equilibrating step before the subsequent rate-limiting step.[16,30] The charge transfer from Mo to Au leads to an electron rich surface of MDA NP that can effectively promote the fast electron transfer to CO_2 molecule as a fast pre-equilibrium step before rate-determining step. These results prove that the Mo doped in Au can change the reaction pathway by the electron rich active sites to further improve the catalytic activity, and this finding is in agreement with previous literature.[31,32]

The CO_2 reduction on MDA NP and Au NP was elucidated using DFT calculations. For the two-electron pathway for CO_2 reduction into CO in Fig. 4a, the formation steps of *COOH, namely, the first protonation step of CO_2 reduction, corresponds to the electrochemical potential-determining step (PDS), which limits the following CO generation. The free energy barrier at the PDS decreased from 1.15 eV for Au(111) to 0.68 eV for Mo-doped Au(111), clearly suggesting that the formation of *COOH is highly favorable on the MDA NP. The doping Mo atom and surrounding Au atoms served as synergetic catalytic sites, in which both of the C–Au and O–Mo binding modes are responsible for stabilizing the *COOH when compared with pristine Au(111) surface. Comparison of the projected density of state (Fig. 4b-c) also indicated that except for the electron density overlap at the energy range below −6 eV for C–Au binding modes, O–Mo binding states were observed at the energy range from −6.0 eV to the Fermi level for Mo-doped Au(111). This result implies that the interaction between Mo and *COOH in Mo-doped Au surface through an additional Mo–O binding can further improve the thermodynamic stability of the *COOH intermediate compared with that in pure Au surface. Thus, obtaining a low energy barrier for CO_2 reduction using MDA NP is reasonable to improve the catalytic performance. Furthermore, we also simulated the CO_2 reduction on Au(110) and Au(322) surfaces accordingly in Fig. S12 and Fig. S13. It was found that the activities of the CO_2 reduction on the stepped surfaces are more active than that of Au(111) due to more exposed unsaturated atoms around the stepped sites, and the Mo-doping effect further stabilized the adsorption of the intermediate *COOH, which results into the second protonation process as the potential-limiting step. Meanwhile, we also want to stress that the Au(111) had the lowest surface energy, indicating that the Au(111) surface is dominant exposed surface[33] for Au nanoparticles although the stepped (110) and (322) surface are more suitable for the CO_2 reduction. Mo-doping on such high energy surfaces could destroy the intrinsic electronic structure and break their original high-performances. By comparison, the Mo-doping effect is helpful for improving the CO_2 reduction on Au(111) surface. Therefore, Mo-doping on Au to improve activity exhibits a dependence on crystal surface, which also confirms the dominating role of Au(111) planes on MDA NP surface to achieve an enhanced activity than Au NP.

Conclusions

In summary, a highly active and stable MDA NP for CO_2 reduction was synthesized using solvothermal method. The charge transfer occurred between two elements by introducing Mo into Au to form electron rich Au sites near Mo atoms. For MDA NP, an impressive FE of 97.5% for CO was achieved at −0.4 V together with a 75-fold higher partial current density versus Au NP for at least 50 h. The improved performance originates from the increased electron density of Au in MDA NP to provide extra affinity for CO_2 activation compared with that in pristine Au surface. Theoretical calculation also revealed that the Mo can help stabilize the *COOH intermediate through an additional Mo–O binding to reduce the energy barrier. These results show that the synergies between the electronic and geometric effects can update the CO_2 reduction performance for the catalyst and thus provide fundamental mechanism insights into alloy electrocatalysts.

Conflicts of interest

The authors declare no conflict of interest.

Acknowledgements

Z.Wang acknowledge financial support from the National Natural Science Foundation of China (No. 51572062). K.Sun is thankful to the China Scholarship Council for providing a scholarship (201906120349). Y.L. acknowledges the support by the National Science Foundation (Grant No. 1900039) and the Welch Foundation (Grant No. F-1959-20180324). The calculations used computational resources at (1) National Renewable Energy Lab (sponsored by the DOE's Office of EERE), (2) the Extreme Science and Engineering Discovery Environment (XSEDE) through allocation TG - CHE190065, (3) the Center for

Nanoscale Materials (a DOE Office of Science user facility supported under Contract No. DE‐AC02‐06CH11357) at Argonne National Lab, and (4) the Center for Nanophase Materials Sciences (a DOE Office of Science user facility) at Oak Ridge National Lab.

Notes and references

1 D. R. Feldman, W. D. Collins, P. J. Gero, M. S. Torn, E. J. Mlawer and T. R. Shippert, *Nature*, 2015, **519**, 339-343.
2 S. Chu, Y. Cui and N. Liu, *Nat Mater*, 2016, **16**, 16-22.
3 G. A. Olah, G. K. Prakash and A. Goeppert, *J Am Chem Soc*, 2011, **133**, 12881-12898.
4 A. Goeppert, M. Czaun, J. P. Jones, G. K. Surya Prakash and G. A. Olah, *Chem Soc Rev*, 2014, **43**, 7995-8048.
5 S. Gao, Y. Lin, X. Jiao, Y. Sun, Q. Luo, W. Zhang, D. Li, J. Yang and Y. Xie, *Nature*, 2016, **529**, 68-71.
6 K. Sun, L. Wu, W. Qin, J. Zhou, Y. Hu, Z. Jiang, B. Shen and Z. Wang, *Journal of Materials Chemistry A*, 2016, **4**, 12616-12623.
7 C. G. Morales-Guio, E. R. Cave, S. A. Nitopi, J. T. Feaster, L. Wang, K. P. Kuhl, A. Jackson, N. C. Johnson, D. N. Abram, T. Hatsukade, C. Hahn and T. F. Jaramillo, *Nature Catalysis*, 2018, **1**, 764-771.
8 Z. Wang, L. Wu, K. Sun, T. Chen, Z. Jiang, T. Cheng and W. A. Goddard, 3rd, *J Phys Chem Lett*, 2018, **9**, 3057-3061.
9 D. D. Zhu, J. L. Liu and S. Z. Qiao, *Advanced materials*, 2016, **28**, 3423-3452.
10 S. Zhu, Q. Wang, X. Qin, M. Gu, R. Tao, B. P. Lee, L. Zhang, Y. Yao, T. Li and M. Shao, *Advanced Energy Materials*, 2018, **8**, 1802238.
11 A. Y. Khodakov, W. Chu and P. Fongarland, *Chemical Reviews*, 2007, **107**, 1692-1744.
12 Q. Lu and F. Jiao, *Nano Energy*, 2016, **29**, 439-456.
13 J. Qiao, Y. Liu, F. Hong and J. Zhang, *Chem Soc Rev*, 2014, **43**, 631-675.
14 A. J. Welch, J. S. DuChene, G. Tagliabue, A. Davoyan, W.-H. Cheng and H. A. Atwater, *ACS Applied Energy Materials*, 2018, **2**, 164-170.
15 N. T. Nesbitt, M. Ma, B. J. Trześniewski, S. Jaszewski, F. Tafti, M. J. Burns, W. A. Smith and M. J. Naughton, *The Journal of Physical Chemistry C*, 2018, **122**, 10006-10016.
16 Y. Chen, C. W. Li and M. W. Kanan, *J Am Chem Soc*, 2012, **134**, 19969-19972.
17 Z. Cao, S. B. Zacate, X. Sun, J. Liu, E. M. Hale, W. P. Carson, S. B. Tyndall, J. Xu, X. Liu, X. Liu, C. Song, J. H. Luo, M. J. Cheng, X. Wen and W. Liu, *Angewandte Chemie*, 2018, **57**, 12675-12679.
18 K. Sun, T. Cheng, L. Wu, Y. Hu, J. Zhou, A. Maclennan, Z. Jiang, Y. Gao, W. A. Goddard, 3rd and Z. Wang, *J Am Chem Soc*, 2017, **139**, 15608-15611.
19 D. Kim, J. Resasco, Y. Yu, A. M. Asiri and P. Yang, *Nat Commun*, 2014, **5**, 4948.
20 E. L. Clark, C. Hahn, T. F. Jaramillo and A. T. Bell, *J Am Chem Soc*, 2017, **139**, 15848-15857.
21 R. Kortlever, J. Shen, K. J. P. Schouten, F. Calle-Vallejo and M. T. M. Koper, *The Journal of Physical Chemistry Letters*, 2015, **6**, 4073-4082.
22 N. J. Firet and W. A. Smith, *ACS Catalysis*, 2017, **7**, 606-612.
23 X. Yuan, L. Zhang, L. Li, H. Dong, S. Chen, W. Zhu, C. Hu, W. Deng, Z.-J. Zhao and J. Gong, *Journal of the American Chemical Society*, 2019, **141**, 4791-4794.
24 Y. Wang, L. Cao, N. J. Libretto, X. Li, C. Li, Y. Wan, C. He, J. Lee, J. Gregg, H. Zong, D. Su, J. T. Miller, T. Mueller and C. Wang, *Journal of the American Chemical Society*, 2019, **141**, 16635-16642.
25 T. B. Massalski, H. Okamoto, P. R. Subramanian and L. Kacprzak, *Binary Alloy Phase Diagrams*, ASM International, 2nd edn., 1990.
26 Z. Liu, J. E. Hu, Q. Wang, K. Gaskell, A. I. Frenkel, G. S. Jackson and B. Eichhorn, *Journal of the American Chemical Society*, 2009, **131**, 6924-6925.
27 X. Huang, Z. Zhao, L. Cao, Y. Chen, E. Zhu, Z. Lin, M. Li, A. Yan, A. Zettl, Y. M. Wang, X. Duan, T. Mueller and Y. Huang, *Science*, 2015, **348**, 1230.
28 H. Mistry, R. Reske, Z. Zeng, Z.-J. Zhao, J. Greeley, P. Strasser and B. R. Cuenya, Journal of the American Chemical Society, 2014, 136, 16473-16476.
29 N. Todoroki, H. Tei, H. Tsurumaki, T. Miyakawa, T. Inoue and T. Wadayama, ACS Catalysis, 2019, 9, 1383-1388.
30 M. Ma, B. J. Trześniewski, J. Xie and W. A. Smith, *Angewandte Chemie International Edition*, 2016, **55**, 9748-9752.
31 Z. Cao, J. S. Derrick, J. Xu, R. Gao, M. Gong, E. M. Nichols, P. T. Smith, X. Liu, X. Wen, C. Copéret and C. J. Chang, *Angewandte Chemie International Edition*, 2018, **57**, 4981-4985.
32 Z. Cao, D. Kim, D. Hong, Y. Yu, J. Xu, S. Lin, X. Wen, E. M. Nichols, K. Jeong, J. A. Reimer, P. Yang and C. J. Chang, *Journal of the American Chemical Society*, 2016, **138**, 8120-8125.
33 L. Vitos, A. V. Ruban, H. L. Skriver and J. Kollár, *Surface Science*, 1998, 411, 186-202.

Entry for the Table of Contents

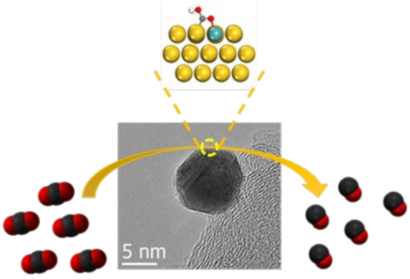

Mo-doped Au catalyst with electron rich Au sites and geometric effect of Mo atom exhibits enhanced activity for CO_2 reduction.